Self-healing of damaged particulate materials through sintering

S. Luding[1,2] and A.S.J. Suiker[3]

1) *Multi Scale Mechanics, TS, CTW, UTwente, P.O. Box 217, 7500 AE Enschede, The Netherlands.*

2) *Particle Technology, Nanostructured Materials, DelftChemTech, TUDelft, Julianalaan 136, 2628 BL Delft, The Netherlands.*

3) *Faculty of Aerospace Engineering, Kluyverweg 1, 2629 HS, Delft, The Netherlands.*

E-mail address of corresponding author: s.luding@utwente.nl

ABSTRACT

Particulate materials loaded under uniaxial compression and tension are studied using the Discrete Element Method (DEM). Self-healing of the damaged samples is activated through sintering, a process that effectively increases the contact adhesion (i.e., the tensile strength) between particles.

The initial sample is prepared from spherical particles by applying high (isotropic) pressure, where particles in contact deform plastically and adhere to each other due to increased van der Waals forces. The result of this pressure-sintering is a solid sample from which the stress is released before uniaxial tension or compression is applied. Damage occurs "microscopically" through loss of contacts and thus loss of adhesion. In order to "self-heal" (part of) this damage, the mechanical loading is stopped. The system is then sintered again, so that the adhesion at existing contacts in the damaged sample becomes stronger than originally. Subsequently, mechanical loading is continued.

The stress-strain curves for the mechanically loaded samples are characterized by a peak-strength followed by a softening branch. Self-healing of an originally "weak" sample, up to a "strong" adhesion level, leads to qualitatively different stress-strain behavior, dependent on the strain at which self-healing is applied. Interestingly, the response of the "weak" self-healed material is bounded by the damage response of the "strong" material. For an optimal self-healing of the particulate material, it is preferable to initiate the healing mechanism during the early stage of damage development, before the peak-strength is reached.

1. Introduction

The self-healing capability of biological systems has recently encouraged researchers to develop engineering materials that are able to heal cracks autonomously. One approach used in the development of self-healing materials is to initiate a bonding reaction at the crack faces, such that the defect disappears and the local load-bearing capacity of the material is re-established. At the molecular level a bonding reaction can be induced increasing the mobility of atoms towards the defect site, where they will occupy the defect volume and bond the crack faces together. The necessary diffusion and bonding characteristics of the "healing atoms" are realized by means of appropriate thermal and/or chemical processes [1]. A well-known example of self-healing through a chemical process has been reported in the original contribution of White et al. [2], who suggest embedding brittle microcapsules filled with a liquid healing agent within an epoxy matrix. When a crack running through the epoxy breaks one of the microcapsules, the liquid flows out of the capsules into the cracked area, and glues the crack faces together when getting into contact with a catalyst. The authors demonstrate that this self-healing concept makes it possible to almost completely recover the original strength of the epoxy matrix. Another self-healing mechanism for polymers can be obtained by controlling the polymer network architecture through the presence of non-covalent hydrogen bonds [3]. The reversibility of the hydrogen bonds may induce a spontaneous rearrangement of principal chemical bonds. This allows the polymer to adjust its configuration to external stimuli, thus providing it with an inherent self-healing capability.

In addition to chemical processes, engineering materials often need an input of external energy, such as heating, in order to trigger self-healing. Varley [4] describes the self-healing behaviour of ionomers after bullet penetration, where the heat required for locally healing the material directly comes from the ballistic impact. Alternatively, self-healing paintings have been introduced recently in the automotive industry, where small scratches generated during car washing vanish after exposure to solar heating. A similar healing mechanism has been applied for developing scratch-free ski goggles, where the scratches disappear when the ski goggles are exposed to heat generated by a standard central heating system. More examples of state-of-the-art self-healing materials can be found in the recently published overview edited by Van der Zwaag [1].

In the present paper the self-healing capacity of damaged particulate materials due to sintering is analyzed. The mechanical response of the particulate material is simulated by means of the Discrete Element Method (DEM), where the discrete masses represent the particles and their interactions are simulated with the sintering contact model of Luding *et al.* [5]. This contact model is able to account phenomenologically for the plastic, adhesive, stress- and temperature effects at the particle contact level, as effectively resulting from diffusion of atoms during sintering. However, for simplicity only the net increase in particle contact strength due to sintering is simulated in this study, without accounting in detail for all microscopic mechanisms involved. Experimental measurements have shown that the net increase in strength depends on the sintering temperature and duration (see for example [6,7,8]). In the simulations it is assumed that during the initial pressure sintering stage, where the particulate sample is prepared, the optimal strength is not reached. Hence, the sample still has the ability to be strengthened further during a *second* sintering (healing) stage, which is applied after the sample has experienced damage under mechanical loading. This damage results from subjecting the particulate system to uniaxial tension or compression, and is characterised by a loss of adhesion at the particle contact level. The question is to which extent the damage can be “healed” by a second sintering cycle, applied at different deformation stages (i.e., at different damage levels).

The paper is organized as follows. In Section 2 the simulation method is presented. The DEM approach is summarized, and the sintering contact model is reviewed. Subsequently, the loading conditions and material parameters used in the DEM simulations are discussed, and the preparation procedure of the particulate sample is explained. In Section 3 the numerical results of the DEM simulations are presented, starting with the damage responses under uniaxial tensile and compressive loadings. The efficiency of self-healing through sintering is studied by applying the sintering process at different stages of mechanical deformation. Finally, in Section 4 some concluding remarks and an application of the present study are given.

2. Simulation method

2.1 DEM modeling of particulate materials

Discrete Element Method (DEM) studies of particle systems illustrate how the macroscopic response, as characterized by the yield strength, stiffness, dilatancy and anisotropy, depends on various microscopic properties, such as the contact network topology and particle size, and the contact adhesion, friction, stiffness and viscosity [9-22]. Most of the above microscopic properties do not remain constant during the loading process, but depend on the actual deformation, stress and temperature of the material sample; for example, in a sintering process the adhesion between particles (strongly) increases with temperature and pressure [5,22].

Depending on the formulations of the particle kinematics and the constitutive behaviour at particle contact level, various links can be established between the micro- and macrostructural characteristics of a particulate structure [9,10,12,13,15,17,19,20,23-26]. In the present study, the coupling between micro- and macro scale properties is performed by first solving the equations of motion at the particle level, in a similar fashion as in the classical molecular dynamics approach, see the textbook [27] by Allen and Tildesley (1987). Subsequently, the effective response of the particle system (expressed in terms of stress and strain) is derived through averaging the local variables at the particle contact level (force and displacement) over the assembly volume. Provided that the particle shape would appropriately be represented in the DEM model, the accuracy of the effective response solely depends on the chosen particle contact model [14,22,28,29]. This makes this approach suitable for accurately predicting experimental results in a relatively straightforward fashion, and carefully judging the validity of macroscopic constitutive models [16,17,19,30]. In addition, a simple approximation of a system of complex-shaped particles by an assembly of spherical grains typically reproduces the qualitative response of the system rather well, even under fairly complicated loading paths [31], although recent studies have demonstrated that the accurate simulation of systems composed of non-spherical particles is also possible [32,33]. Nonetheless, for reasons of simplicity, in the present study systems of spherical particles are considered.

2.2 Sintering contact model

The particulate samples used in the present study are (i) *prepared* and (ii) *self-healed* through the application of a sintering process. For this purpose, the non-linear sintering contact model recently proposed by Luding *et al.* [5] and Luding [22,29] is used. (For the interested reader, these references can provide much more detail than the discussion below.) As sketched in Fig. 1, the *normal contact* *force f* directed parallel to the line connecting the centers of two contacting particles is governed by the evolution of the contact overlap, $\delta > 0$. If $\delta < 0$, there is no contact between particles, and thus $f = 0$. The sign convention is such that positive (*negative*) values of the contact displacement δ relate to particle overlap (*separation*) and positive (*negative*) values of the contact force f relate to compression (*tension*).

During initial compressive loading, the contact force increases proportionally with the contact overlap as $f = k_1\delta$, where k_1 is the elasto-plastic contact stiffness. At a specific maximum contact overlap δ_{max}, the contact stiffness increases instantaneously to a value k_2. Further loading as well as unloading are defined by the force-displacement relation $f = k_2(\delta - \delta_f)$. Elastic unloading to a zero contact force leads to a contact overlap equal to the maximum plastic contact indentation, $\delta = \delta_f$. When the contact overlap is further decreased, the contact force enters the tensile regime, with the maximum tensile contact force $f_{t,\mathrm{max}} = -k_t\delta_{t,\mathrm{max}}$ corresponding to a contact displacement $\delta = \delta_{t,\mathrm{max}}$. The final part of the tensile regime is characterized by an unstable softening branch, with the tensile contact force dropping from its maximum value towards zero in accordance with $f = -k_t\delta$. For the sake of brevity, the tensile softening parameter k_t hereafter is referred to as the "contact adhesion". In addition to the loading and unloading branches reflected by the outer triangle in Fig. 1 (Right), loading and unloading may also occur within this triangle, as characterised by a branch with stiffness k_* that follows from a linear interpolation of the stiffnesses k_1 and k_2.

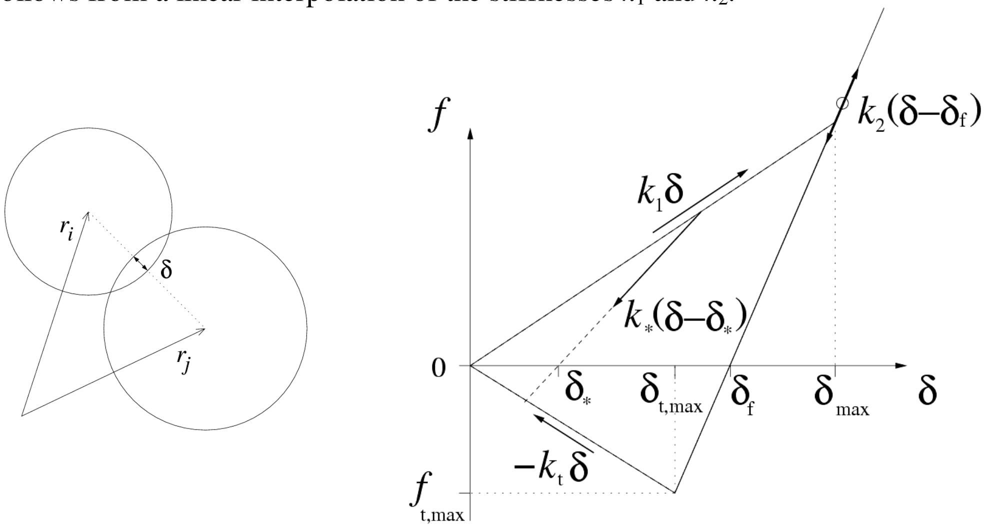

Fig. 1 (Left) Two-particle contact with contact overlap δ. (Right) Particle contact model in terms of the normal contact force plotted against the contact overlap (compression is assumed positive). For more details, see [5,22,29].

In summary, the model has three ("stiffness") k-parameters in the model describe three physical effects like (1) elasticity, (2) plastic deformation, (3) contact-adhesion. Furthermore, the model involves (4) nonlinear contact stiffness via the choice of k_*. This piece-wise linear model is a compromise between simplicity and the need to model physical effects. There is no literature available to our knowledge that provides detailed information involving all four physical contact properties above and their nonlinear, history-dependent behavior. If this information becomes available, the present model can be extended and generalized.

The *tangential contact force* parallel to the particle contact plane is related to the tangential contact displacement by means of a linear elastic contact law, with the tangential stiffness equal to k_s. The tangential contact displacement depends both on the translations and rotations of the contacting particles. A Coulomb friction law determines the maximum value of the tangential contact force: During sliding the ratio between the tangential contact force and the normal contact force is assumed to be limited and equal to a (constant) friction coefficient μ. In a similar fashion, the elastic contact behaviour related to rolling and twisting (torsion) is set by elastic constants k_r and k_o, respectively, and the maximum values of the corresponding contact torques depend on the normal contact force through a Coulomb-type law with "friction" coefficients μ_r and μ_o, respectively. More details on the contact model can be found in Refs. [5,22,29].

The overall solution of the non-linear DEM problem is obtained by incrementally solving Newton's equations of motion for the translational and rotational particle degrees of freedom. In the case of short-range particle interactions, which are present in particulate media such as powders and sands, a considerable decrease in computational time can be achieved using a linked-cell method that allows for a more efficient particle neighborhood search. Hence, this procedure is applied for the present simulations, and more details on the algorithm can be found in, for example Ref. [27].

2.3 Loading conditions and material parameters

The DEM simulations consist of four subsequent stages, namely (i) a sample preparation stage, (ii) a uniaxial (tensile or compressive) loading stage, (iii) a self-healing stage, and (iv) a continuation of the uniaxial (tensile or compressive) loading stage. The samples used in the study are composed of 1728 poly-dispersed, spherical particles. The radii R_i of the particles are drawn from a Gaussian distribution around a mean value $\overline{R} = 0.005$ mm [18,22]. Six outer walls forming a cuboidal volume with side lengths of 0.115 mm prescribe the geometry of the sample. The overall size of the sample was – at least for adhesionless particles – large enough to show only weak boundary effects. The issue of a statistically representative volume element (RVE) is far from the scope of this first paper, so that we chose a system where the computational time remains manageable. More detailed studies of the system size, different compression rates and also different (local) sintering procedures are in progress [34].

The sample preparation is carried out subjecting a loose assembly of particles to (*isotropic) pressure sintering* (as discussed below in more detail), such that a coherent and solid particulate sample is obtained that can be subsequently subjected to a *uniaxial tensile* or *uniaxial compressive* test. In a uniaxial compressive test, one of the two outer walls, with its normal parallel to the axial (loading) direction, is slowly moved towards the opposite wall. The change of the wall displacement in time is prescribed by a cosine function. The time period of the cosine function is taken relatively large in order to limit inertia effects [14,16,19]. Uniaxial tension is applied in a similar fashion as uniaxial compression, i.e., one of the two outer walls is slowly moved away from the opposite wall. Here, the connection between the "boundary particles" and the walls is warranted through using an artificially large contact adhesion k_t at the two walls with normals in loading direction. After some deformation, the sample has experienced a certain amount of fracture. The uniaxial loading then is temporarily stopped, and self-healing is activated. The self-healing is achieved by an instantaneous increase of the particle contact adhesion k_t, see Fig. 2, which is assumed to be the net effect of a sintering cycle. Observe from Fig. 2 that an increase of the contact adhesion k_t corresponds to an increase of the maximum tensile strength $f_{t,max}$, and a decrease of the corresponding displacement $\delta_{t,max}$.

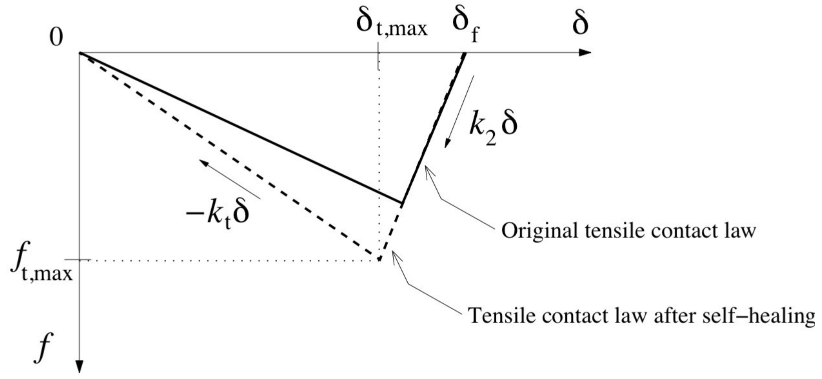

Fig. 2 The particle contact law in the tensile regime, before (solid line) and after (dashed line) self-healing through sintering has been applied.

After the application of the sintering cycle, the uniaxial loading is resumed, where the effect of self-healing on the effective stress-strain response of the sample becomes apparent through a comparison of its response with that of the unhealed, reference sample.

The material simulated represents a fine, stiff adhesive powder, with a particle size in the order of a few micrometers. The particle density used in the simulations is ρ=2000 kg/m^3. The maximum elastic contact stiffness is k_2=5.10^4 N/m, which determines the response time scale, $t_c=\pi\big/\sqrt{k_2/m}$, of particles with mass m. The initial elasto-plastic stiffness (normalized by k_2) is k_1/k_2=1/2, and the contact adhesion k_t/k_2 is varied in the simulations. The maximum plastic contact indentation for two contacting particles with radii R_1 and R_2 is computed as $\delta_f = \phi_f\ 2R_1R_2/(R_1+R_2)$, with the maximum plastic indentation strain equal to $\phi_f = 0.05$.

The tangential stiffness, rolling stiffness and twisting stiffness have the (normalized) values k_s/k_2=1/5, k_r/k_2=1/10, and k_o/k_2=1/10, respectively, and the friction coefficients corresponding to these deformation modes are μ=1.0, μ_r =0.0 and μ_o=0.0. In order to account for velocity-dependent dissipation and to limit the computational time necessary for reaching static equilibrium, the model is extended with viscous damping, with the damping coefficient in the normal direction being equal to γ = 5 kg/s, and the tangential, rolling and twisting damping (expressed in the same units as the normal contact damping) equal to γ_s / γ = 1/5, γ_r / γ =1/10 and γ_o / γ = 1/10, respectively. Furthermore, translational and rotational background viscosities are introduced when computing the overall forces and torques acting on individual particles. This is done in order to efficiently dissipate dynamic response contributions related to relatively long wavelengths. The values of the translational and rotational background viscosities are $\gamma_b / \gamma = 4$ and $\gamma_{br} / \gamma = 1$, respectively. When the loading rate is set a factor of two lower, the change in the peak strength is small – thus it is assumed that the response is close to the quasi-static limit. More explanations and studies of the above material parameters can be found in [22,29]. Note however that the choice of parameters is empirical – most of them are chosen and kept fixed while the effect of a few (presumably most relevant for sintering) is studied.

From the viewpoint of computational efficiency the incremental time step used in the DEM simulations should be as large as possible; however, in practice the magnitude of the time-step is limited by numerical stability requirements. The *critical time-step* for numerical stability can be estimated from the response period of a linear spring-dashpot-mass system subjected to an initial displacement [11,22]. With this procedure, the integration time step has been determined as $\Delta t = 5.10^{-10}$ s, which is about 100 times smaller than this response period t_c. The present choice of the time step warrants the stability of the numerical procedure under arbitrary loading conditions and deformation paths.

2.4 Sample preparation

As already mentioned briefly, the sample is prepared subjecting the particulate structure to a *pressure sintering* process, which is characterized by two stages. The first stage reflects the application of a hydrostatic (or isotropic) pressure $p_s / \sigma_0 = 10^{-2}$ (with the reference stress $\sigma_0 = k_2 / \bar{R}$, where $\bar{R} = 0.005$ mm is the average particle radius) to a loose assembly of particles. The desired stress is applied to the six outer walls; see e.g. Ref. [14] for more details. In the normal direction of the particle contacts, the particles deform plastically as a result of the relatively large value of the hydrostatic stress p_s. In the tangential direction and the rolling directions of the particle contacts, the particles are subjected to sliding when the contact frictional resistance is exceeded, where the friction coefficients are in accordance with the values mentioned in Section 2.3. The walls are considered to be virtually frictionless, i.e., $\mu_{wall} = 0.01$. The contact adhesion is set to zero ($k_t/k_2 = 0$) for all particle-wall contacts, except for the particle-wall contacts in the direction of the uniaxial loading applied later (i.e., after the sample preparation phase has finished). For these walls, a relatively high contact adhesion of $k_t/k_2=20$ is used in order to force the “wall particles” to directly follow the prescribed uniaxial deformation. The other contact parameters have the same values as mentioned in Section 2.3. During the application of the hydrostatic pressure, the value of the particle contact adhesion hardly affects the response, since most particles are loaded in compression. In fact, additional simulations not presented here have shown that virtually identical simulation results are obtained for contact adhesion values in the range $0 < k_t/k_2 < 0.5$. The hydrostatic loading process is considered to be finished when the kinetic energy of the sample is negligible compared to the potential energy. The solid volume fraction at the end of the hydrostatic loading process is $\nu = 0.676$ (which relates to a porosity of $1-\nu = 0.324$), and the average particle coordination number is $C = 7.17$.

The second stage of the pressure sintering process is reflected by a *stress relaxation* phase, where the adhesion at *all* particle contacts is increased to $k_t/k_2 = 1/5$, and the external hydrostatic pressure is reduced to virtually zero, $p_s / \sigma_0 = 10^{-5}$.

Due to the presence of a particle contact adhesion, the lateral stability of the specimen remains preserved when the hydrostatic pressure is released; i.e., a coherent and stable particulate structure is obtained that can be subsequently used in the analysis of damage and healing under uniaxial loading conditions. The solid volume fraction of the sample after stress relaxation is $\nu = 0.63$ and the coordination number is $C = 6.09$.

3. Numerical results

3.1 Damage response under uniaxial loading

The responses of the sample under uniaxial compression and uniaxial tension are shown in Fig. 3 (Left). The normal axial stress σ (normalized by the reference stress $\sigma_0 = k_2/\overline{R}$) is plotted as a function of the normal axial strain ε, where positive stress (*strain*) values relate to compression (*contraction*). The stress-strain curves are depicted for different values of k_t (normalized by k_2), which quantifies the adhesion at the particle contacts, see Figs. 1 and 2, and thus when changing k_t the self-healing potential of the material. It can be observed that a larger particle contact adhesion increases the effective strength of the sample, both under uniaxial tension and compression. Furthermore, the overall strain at which the effective stress reaches its maximum increases with increasing value of k_t. Observe that the maximum stress under uniaxial compression is about 5 times larger than under unaxial tension. A relatively high compressive strength in relation to the tensile strength is typical of various sintered materials, such as ceramics [35].

As can be further noticed from Fig. 3, the softening branch under uniaxial tension is somewhat steeper than under uniaxial compression. For larger compression rates, the system displays strong dynamic effects while for much smaller rates, the peak strength is not changed much for tension, but reduced a few per-cent for compression. Thus we use a rate here that is close to the quasi-static regime, as studied in more detail by [34].

The initial (elastic) axial stiffnesses C_t in tension and compression are determined by the sample preparation procedure, and are approximately equal for all the cases considered here, i.e., $C_t/\sigma_0 = 0.26$. The quantity C_t can be used to compare the present data with real experiments. All tensile responses plotted in Fig. 3 (Right) are characterized by local failure at the center of the sample. However, additional simulations not presented here have shown that local failure may also occur nearby one of the outer walls in the axial direction if the particle adhesion is equal or higher than the value $k_t/k_2=20$ used for the “wall particles”. In addition, changing the rolling and twisting friction parameters from $\mu_r = \mu_o = 0.0$ to $\mu_r = \mu_o = 0.2$ increased the tensile peak strength of the sample with about 20%, but a further increase of these friction parameters altered the tensile stress-strain response only little, see Ref. [22] for details.

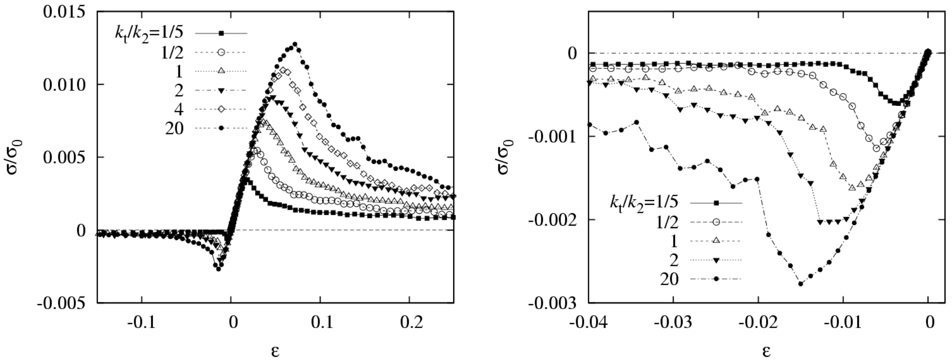

Fig. 3 (Left) Axial stress versus axial strain during uniaxial compression (positive stress and strain values) and uniaxial tension (negative stress and strain values), for different particle contact adhesions k_t (normalized by k_2). (Right) Magnification of the tensile responses plotted in the left figure.

3.2 Self-healing under uniaxial compression

Under uniaxial compression the self-healing behaviour of the initial sample with $k_t/k_2 = 1/5$ is simulated by instantaneously increasing the contact adhesion to $k_t/k_2 = 1$. The self-healing mechanism is activated uniformly at all particle contacts, and is initiated at different deformation levels of the sample. Fig. 4 shows the response curves after the initiation of self-healing (dashed lines, labeled with the abbreviation ‘SH’), together with the stress-strain responses of the relatively weak ($k_t/k_2 = 1/5$, solid squares) and strong ($k_t/k_2 = 1$, triangles) samples, taken from Fig. 2. Note that the maximum compressive strength reached after self-healing is larger if self-healing is initiated at smaller axial deformation. Furthermore, for all self-healing cases considered the response eventually converges with the damage response of the “strong” sample with $k_t/k_2 = 1$. This is, because the damage response of the strong sample essentially may be interpreted as the response of a “self-healed” sample where the increase in contact adhesion to $k_t/k_2 = 1$ is initiated at the onset of mechanical loading. Consequently, the failure response of the sample with $k_t/k_2 = 1$ acts as an envelope for the failure responses of the self-healed samples with k_t/k_2 increased from 1/5 to 1 at any deformation level.

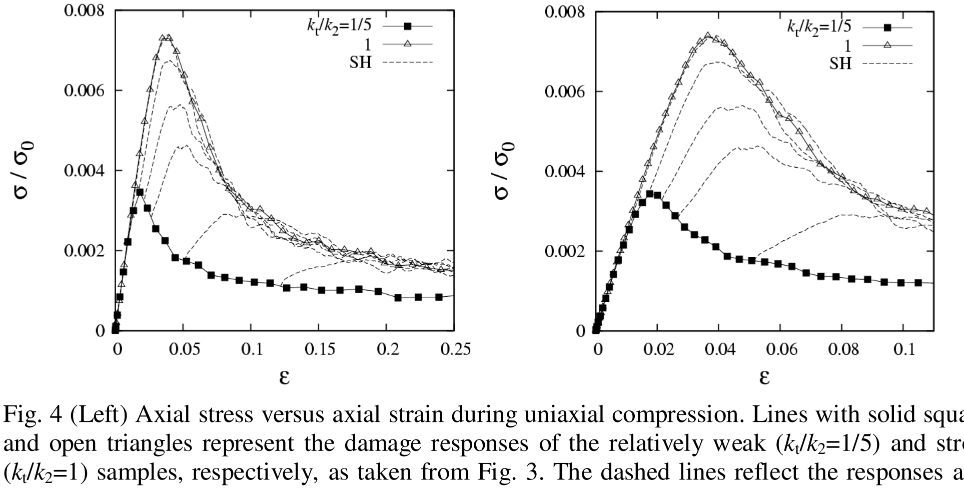

Fig. 4 (Left) Axial stress versus axial strain during uniaxial compression. Lines with solid squares and open triangles represent the damage responses of the relatively weak (k_t/k_2=1/5) and strong (k_t/k_2=1) samples, respectively, as taken from Fig. 3. The dashed lines reflect the responses after the initiation of self-healing (which occurs by increasing the particle contact adhesion to $k_t k_2$=1) at various deformation levels. (Right) Magnification of the responses plotted in the left figure; the initiation of self-healing occurs at axial strains $\varepsilon \approx 0.016, 0.019, 0.022, 0.026, 0.045$, and 0.12.

3.3 Self-healing under uniaxial tension

In the case of uniaxial tension, self-healing is investigated by increasing the contact adhesion at various deformation levels from $k_t/k_2 = 1/5$ to $k_t/k_2 = 1$ (Fig. 5, Left) and to $k_t/k_2 = 20$ (Fig. 5, Right). Similar to the self-healing responses under uniaxial compression (see Fig. 4), the maximum tensile strength of a self-healed sample is larger if self-healing is initiated at lower axial deformation. Furthermore, the responses of the self-healed samples eventually coincide with the damage responses of the relatively "strong" sample with $k_t/k_2 = 1$ (Fig. 5, Left) and the "very strong" sample with $k_t/k_2 = 20$ (Fig. 5, Right). A comparison of the self-healing curves in Figs. 5 (Left) and (Right) shows that a stronger increase in contact adhesion clearly gives rise to a higher overall sample strength, and thus to an improved self-healing performance.

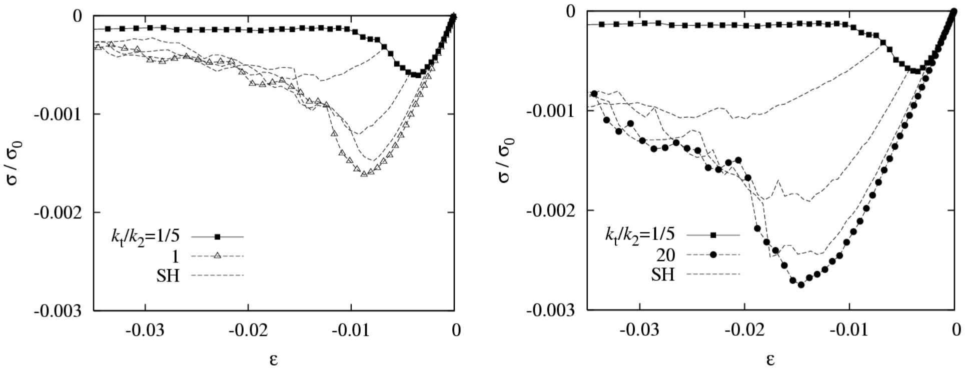

Fig. 5 Axial stress versus axial strain during uniaxial tension. The lines with solid squares, open triangles, and solid circles represent the damage responses of the relatively "weak" (k_t/k_2=1/5), "strong" (k_t/k_2=1) and "very strong" (k_t/k_2=20) samples, respectively, as taken from Fig. 3. The dashed lines reflect the responses after the initiation of self-healing, which occurs by increasing the contact adhesion to k_t/k_2=1 (Left) and k_t/k_2=20 (Right) at various deformation levels ($\varepsilon \approx -0.005$, -0.006 and -0.007).

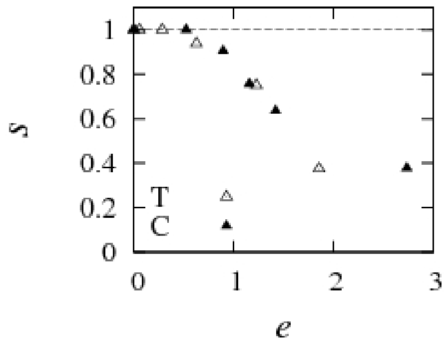

Fig. 6 Self-healing strength *s* plotted against the self-healing strain *e*, for the uniaxial compressive (C) and tensile (T) tests – see text for the definitions of *s* and *e*.

In order to quantify the efficiency of self-healing, a dimensionless healing strength, $s=\sigma_{SH}/\sigma_{max}$, and healing strain, $e=\varepsilon_{SH}/\varepsilon_{max}$ are introduced. Here, ε_{SH} is the strain at which self-healing is initiated and ε_{max} is the strain at which the reference sample without self-healing reaches its peak strength. Further, σ_{SH} and σ_{max} are the peak strengths of the self-healed sample and the reference sample, respectively. In Fig. 6 the self-healing strength *s* is plotted against the self-healing strain *e*, using the data presented in Figs. 4 and 5 (Left), where the particle contact strength after self-healing is $k_t/k_2 = 1$. It can be observed that the self-healing strength is maximal for small strains, i.e., $s \approx 1$ for $e<0.5$, and gradually drops to a value of about 0.4 for strain values between $0.5<e<1.5$. Accordingly, in order to (almost) recover the maximum strength of the original reference sample, self-healing needs to be activated early in the fracture process. Interestingly, the differences between the data for the uniaxial compression (solid triangles) and tension (open triangles) tests are rather small, especially during the early stage of deformation. In other words, the self-healing efficiency only marginally depends on the direction of uniaxial loading. Nonetheless, for deformations $e>1.5$ a noticeable difference can be expected between the two responses plotted in Fig. 6. This is, since samples loaded under uniaxial compression asymptote to a finite, residual strength under continued deformation, whereas samples loaded in uniaxial tension will eventually break completely, thus having zero residual strength. Hence, under continued compression, the asymptotic value for the healing strength σ_{SH} will be finite, whereas it is zero under continued tension.

4. Concluding remarks and application

Self-healing processes in damaged particulate materials have been studied under uniaxial compression and uniaxial tension using DEM simulations. The self-healing is generated through a (global) sintering process, as modeled by increasing the particle contact adhesion from relatively "weak" to relatively "strong". The stress-strain response obtained from self-healed samples eventually converges to the envelope curve that represents the damage response of a sample that has the "strong" contact adhesion since the onset of loading. This feature is independent of the deformation level at which the self-healing mechanism is activated, a property that can be tested experimentally in order to challenge our model: For which class of materials one can observe the same behavior? Furthermore, this is a reference-result for new/different sintering models: Does the model reach the envelope curve, or (as a challenge) is there a self-healing mechanism/model that can do better?

An important outcome of the simulations is that the maximum sample strength reached after self-healing very much depends on the deformation level at which self-healing is activated: If self-healing is activated before the peak-stress is reached, the maximum sample strength will be (virtually) equal to peak strength of the envelope curve. In contrast, if self-healing is initiated in the softening regime, the sample strength may be considerably smaller than the maximum strength following from the envelope curve. Hence, for an optimal strength increase, the healing mechanism should be activated during the early stage of damage growth, before the sample reaches its peak strength.

The approach taken in the present study is relatively straightforward, in a sense that the self-healing mechanism is instantaneously activated at a specific deformation level, and is applied uniformly across the specimen (i.e., at all particle contacts). More refined analyses will be presented in forthcoming work, where the self-healing mechanism is applied *only* at particle contacts experiencing severe damage, and the influence of more parameters like the sensitivity and healing repetition rate will be investigated [34].

An application of the present study relates to increasing the durability of thermal barrier coating (TBC) systems used for the thermal protection of gas turbine engines, thereby allowing these engines to operate at higher temperatures. Currently the lifetime of TBC systems is limited by failure of the brittle ceramic top coating, which occurs through continuous development and coalescence of thermally induced cracks, eventually leading to spallation of parts of the coating [36]. In order to reduce ultimate failure by spallation and to increase the lifetime of TBC systems, new self-healing TBC systems are currently being studied [37], where one of the promising concepts focuses upon the local healing of cracks in the ceramic top coating through sintering at high operational temperatures. If the self-healing mechanism examined in the present study is adequately applied within a TBC system, it may lead to a substantial improvement of the overall thermo-mechanical performance of a turbine engine.

ACKNOWLEDGEMENTS

The authors acknowledge the financial support from the Delft Centre for Materials (DCMat) in the form of project TCO501, “Modelling of repeated self-healing processes in materials”. Furthermore, the helpful discussions with Prof. S. van der Zwaag (Delft University of Technology) on self-healing materials, Dr. W.G. Sloof (Delft University of Technology) on thermal-barrier coating systems and Dr. L. Brendel (University Essen-Duisburg) on particle contact laws are gratefully acknowledged.

REFERENCES

[1] S. Van der Zwaag, *An introduction to material design principles: Damage prevention versus damage management*. in: *Self Healing Materials. An Alternative Approach to 20 centuries of Materials Science*, S. Van der Zwaag, ed., Springer, Dordrecht, The Netherlands, 2007, pp. 1-18.

[2] S. R. White, N. R. Sottos, P. H. Geubelle, J. S. Moore, M. R. Kessler, S. R. Sriram, E. N. Brown, S. Viswanathan, *Autonomic healing of polymer composites*, Nature **409** (2001) pp. 794-797.

[3] R. P. Sijbesma, F. H. Beijer, L. Brunsveld, B. J. B. Folmer, J. H. K. Hirschberg, R. F. M. Lange, J. K. L. Lowe, and E. W. Meijer, *Reversible polymers formed from self-complementary monomers using quadrupole hydrogen bonding*, Science **278** (1997) pp. 1601-1604.

[4] R. Varley, *Ionomers as self healing polymers* in: *Self Healing Materials. An Alternative Approach to 20 centuries of Materials Science*, S. Van der Zwaag, ed., Springer, Dordrecht, The Netherlands, 2007, pp 95-114.

[5] S. Luding, K. Manetsberger, and J. Muellers, *A discrete model for long time sintering*, Journal of the Mechanics and Physics of Solids **53/2** (2005) pp. 455-491.

[6] G. A. Shoales, and R. M. German, *In situ strength evolution during the sintering of bronze powders*, Metallurgical and Materials Transactions A **29a** (1998) pp. 1257-1263.

[7] T. Takeuchi, I. Kondoh, N. Tamari, N. Balakrishnan, K. Nomura, H. Kageyama, Y. Takeda, *Improvement of mechanical strength of 8 mol % Yttria-stabilized zirconia ceramics by spark-plasma sintering*, Journal of The Electrochemical Society **149** (2002) pp. A455-A461.

[8] E. Pirhonen, L. Moimas, and P. Väänänen, *Porous bioactive glass scaffold with high compression strength*, European Cells and Materials **12** (2006) Suppl. 1, pp. 67.

[9] C. S. Chang, and C. L. Liao, *Constitutive relation for a particulate medium with the*

effect of particle rotation, International Journal of Solids and Structures **29** (1990) pp. 437-453.

[10] C. S. Chang, *Micromechanical modeling of deformation and failure for granulates with frictional contacts*, Mechanics of Materials **16** (1993) pp. 13-24.

[11] H. J. Herrmann, J. P. Hovi, and S. Luding (eds.) *Physics of Dry Granular Media*, NATO ASI Series E 350, Kluwer Academic Publishers, Dordrecht, Netherlands, 1998.

[12] C. L. Liao, T. C. Chan, A. S. J. Suiker, and C. S. Chang, *Pressure-dependent elastic moduli of granular assemblies*, International Journal for Numerical and Analytical Methods in Geomechanics **24** (2000) pp. 265-279.

[13] P. A. Vermeer, S. Diebels, W. Ehlers, H. J. Herrmann, S. Luding, and E. Ramm, (eds.) *Continuous and Discontinuous Modelling of Cohesive Frictional Materials*, Lecture Notes in Physics 568, Springer, Berlin, 2001.

[14] S. Luding, and H. J. Herrmann, *Micro-Macro Transition for Cohesive Granular Media*, in: *Zur Beschreibung komplexen Materialverhaltens*, Institut für Mechanik, S. Diebels (Ed.), Stuttgart, 2001, pp 121-134.

[15] A. S. J. Suiker, A. V. Metrikine, and R. de Borst, *Comparison of the wave propagation characteristics of the Cosserat continuum model and corresponding discrete lattice models*, International Journal of Solids and Structures **38** (2001) pp. 1563-1583.

[16] S. Luding, *Micro-macro transition for anisotropic, frictional granular packings*, International Journal of Solids and Structures **41** (2004) 5821-5836.

[17] A. S. J. Suiker, and N. A. Fleck, *Frictional collapse of granular assemblies*, Journal of Applied Mechanics **71** (2004) pp. 350-358.

[18] C. T. David, R. Garcia-Rojo, H. J. Hermann, and S. Luding, *Hysteresis and Creep in Powders and Grains*, in: *Powders and Grains 2005*, R. Garcia Rojo, S. McNamara, and H. J. Herrmann (eds.), Balkema, 2005, pp. 291-294.

[19] S. Luding, *Anisotropy in cohesive, frictional granular media*, Journal of Physics: Condensed Matter **17** (2005) pp. S2623-S2640.

[20] A. S. J. Suiker, and R. de Borst, *Enhanced continua and discrete lattices for modeling granular assemblies*, Philosophical Transactions of the Royal Society A **363** (2005) pp. 2543-2580.

[21] O. Mouraille, W. A. Mulder, and S. Luding, *Sound wave acceleration in granular materials*, Journal of Statistical Mechanics- Theory and Experiment P07023 (2006).

[22] S. Luding, *Cohesive, frictional powders: contact models for tension*, Granular Matter **10** (2008) pp. 235-246.

[23] A. S. J. Suiker, C. S. Chang, and R. de Borst, *Micro-mechanical modeling of granular material. Part 1: Derivation of a second-gradient micro-polar constitutive theory*, Acta Mechanica **149** (2001) pp. 161-180.

[24] A. S. J. Suiker, C. S. Chang, and R. de Borst, *Micro-mechanical modeling of granular material. Part 2: Plane wave propagation in infinite media*, Acta Mechanica **149** (2001) pp. 181-200.

[25] A. V. Metrikine, and H. Askes, *One-dimensional dynamically consistent gradient elasticity models derived from a discrete microstructure. Part 1. Generic formulation.* European Journal of Mechanics A/Solids **21** (2002) pp. 555-572.

[26] H. Askes, and A. V. Metrikine, *One-dimensional dynamically consistent gradient elasticity models derived from a discrete microstructure. Part 2. Static and dynamic response*, European Journal of Mechanics A/Solids **21** (2002) pp. 573-588.

[27] M. P. Allen, and D. J. Tildesley, *Computer simulation of liquids*, Oxford University Press Inc., New York, 1987.

[28] J. Tomas, *Assessment of mechanical properties of cohesive particulate solids – part 1: particle contact constitutive model*, Particle Science Technology **19** (2001) 95-110.

[29] S. Luding, *About contact force-laws for cohesive frictional materials in 2D and 3D*, in:

Behavior of Granular Media, P. Walzel, S. Linz, Ch. Krülle, and R. Grochowski (eds.), Band 9, Schriftenreihe Mechanische Verfahrenstechnik, ISBN 3-8322-5524-9, Shaker Verlag, Aachen, 2006, pp. 137-147.

[30] C. Thornton, and L. Zhang, *A numerical examination of shear banding and simple shear non-coaxial flow rules*, Philosophical Magazine **86** (2006) 3425-3452.

[31] C. Thornton, and S. J. Antony, *Quasi-static deformation of a soft particle system*, Powder Technology **109** (2000) 179-191.

[32] F. Alonso-Marroquin, S. Luding, H. J. Herrmann, and I. Vardoulakis, *Role of anisotropy in the elastoplastic response of a polygonal packing*, Phys. Rev. E **71** (2005) 051304.

[33] G. A. D'Addetta, F. Kun, E. Ramm, *On the application of a discrete model to the fracture process of cohesive granular materials*, Granular Matter **4/2** (2002) pp. 77-90.

[34] O. Herbst, and S. Luding, *Modelling particulate self-healing materials and application to uniaxial compression*, submitted to Int. J. Fracture 2008.

[35] W. E. Lee, and W. M. Rainforth, *Ceramic Microstructures, Property Control by Processing,* Chapman and Hall, London, 1995.

[36] A. G. Evans, D. R. Mumm, J. W. Hutchinson, G. H. Meier, and F. S. Pettit, *Mechanisms controlling the durability of thermal barrier coatings*. Progress in Materials Science **46** (2001) pp. 505-553.

[37] W. G. Sloof, *Self healing in coatings at high temperatures*, in: *Self Healing Materials. An Alternative Approach to 20 centuries of Materials Science.* S. Van der Zwaag, ed., Springer, Dordrecht, The Netherlands, 2007, pp. 309-322.